Circular-Polarization-Selective Transmission Induced by Spin-Orbit Coupling in a Helical Tape Waveguide

Yahong Liu,[1,2,*] Qinghua Guo,[2,3] Hongchao Liu,[2] Congcong Liu,[1] Kun Song,[1] Biao Yang,[2] Quanwen Hou,[1] Xiaopeng Zhao,[1] Shuang Zhang,[2] and Miguel Navarro-Cía[2,†]

[1]*Department of Applied Physics, Northwestern Polytechnical University, Xi'an 710129, China*
[2]*School of Physics and Astronomy, University of Birmingham, Birmingham, Edgbaston B15 2TT, United Kingdom*
[3]*College of Optoelectronic Engineering, Shenzhen University, Shenzhen 518060, China*

(Received 2 October 2017; revised manuscript received 9 January 2018; published 22 May 2018)

Spin-orbit coupling of light, describing the interaction between the polarization (spin) and spatial degrees of freedom (orbit) of light, plays an important role in subwavelength scale systems and leads to many interesting phenomena, such as the spin Hall effect of light. Here, based on the spin-orbit coupling, we design and fabricate a helical tape waveguide (HTW), which can realize a circular-polarization-selective process. When the incident circularly polarized wave is of the same handedness as the helix of the HTW, a nearly complete transmission is observed; in contrast, a counterrotating circular polarization of incident wave results in a much lower transmission or is even totally blocked by the HTW. Indeed, both simulations and experiments reveal that the blocked component of power leaks through the helical aperture of the HTW and forms a conical beam analogous to helical Cherenkov radiation due to the conversion from the spin angular momentum to the orbital angular momentum. Our HTW structure demonstrates its potential as a polarization selector in a broadband frequency range.

DOI: 10.1103/PhysRevApplied.9.054033

I. INTRODUCTION

Spin-orbit coupling (SOC), also called spin-orbit interaction, is an interaction between the spin and motion of a particle. Similar to the SOC of electrons in solids and quantum gases [1–5], light carries both spin angular momentum (i.e., circular polarization) and orbital angular momentum (i.e., spatial degrees of freedom of light), and its SOC can appear when light-carrying intrinsic angular momentum interacts with a medium [6,7]. Having been widely studied in bianisotropic and inhomogeneous metamaterials [8–10], plasmonic metalenses [11], metasurfaces [12–15], etc., the SOC was demonstrated to accurately control and distinguish the polarization of light [16–21]. In addition, the SOC of light leads to a number of interesting phenomena, including the spin Hall effect [6,22,23], spin-controlled shaping and control of light [24–28], and robust spin-directional coupling via evanescent near fields [29–34]. Among them, a controlled steering Cherenkov wake determined by the photon spin angular momentum of the incident radiation was realized in a one-dimensional metamaterial recently [35].

Cherenkov radiation occurs when a charged particle enters an ordinary medium at a velocity higher than the velocity of light in such a medium. Cherenkov radiation has already been widely applied in high-energy physics such as detectors in particle physics [36] and microwave generation [37,38]. There have been also numerous investigations on the generation of Cherenkov radiation and reversed Cherenkov radiation in metamaterials [39–46]. As a specific Cherenkov radiation, the helical Cherenkov radiation effect is a very interesting physical phenomenon, which could possibly be used as a detector of radiation by energetic electrons that are trapped in a medium by strong magnetic fields. Helical Cherenkov radiation was first theorized by Soln [47,48]. Soln demonstrated that the helical Cherenkov radiation can be observed only in the visible spectrum when an external magnetic field value is larger than 100 T [48]. Because of this extreme condition, helical Cherenkov radiation is rarely observed in experiment.

Here, we design and fabricate a helical tape waveguide (HTW) with circular-polarization-selective transmission induced by the SOC. Our simulations and proof-of-concept experiments show that when a right-handed circularly polarized (RCP) electromagnetic wave is incident into the HTW, a nearly complete transmission is obtained. On the contrary, when a left-handed circularly polarized (LCP) wave is incident, HTW behaves as a leaky-wave helical antenna with a conical radiation pattern [49,50] akin

*To whom all correspondence should be addressed. yhliu@nwpu.edu.cn
†To whom all correspondence should be addressed. m.navarro-cia@bham.ac.uk

to a vortex radiation. Originated from the strong SOC (i.e., spin angular momentum to orbital angular momentum conversion), this leaky vortex radiation for LCP is in analogy to a helical Cherenkov radiation. Our HTW demonstrate the results at microwave frequencies; nevertheless, the proposed structure can be scalable to other frequency ranges, given its simplicity.

II. DESIGN AND THEORETICAL ANALYSIS

The configuration and the dimensions of the HTW are shown in Fig. 1(a). We study first the electromagnetic behavior of the HTW by numerical simulations. To this end, the transient solver of the commercial software CST Microwave Studio® is used. Open boundary conditions are applied in all directions, ensuring a convergence of the results. Metal is a perfect electric conductor. The solver-defined adaptive grid is employed with a convergence accuracy of 0.001. A circularly polarized (CP) electromagnetic wave propagating along the $-z$ direction is excited at one end of the HTW using the software-defined waveguide port, whereby two degenerate orthogonal linear modes ($TE_{\perp}$ and $TE_{\parallel}$) with equal amplitude and $\pm 90°$ phase difference are excited ($+90°$ for RCP and $-90°$ for LCP) within the HTW. Another waveguide port is defined at the other end of the HTW to calculate the transmission coefficient S_{21}. The total fields inside the whole simulation volume as well as the radiation characteristic are recorded with the software-defined E-field and far-field monitors.

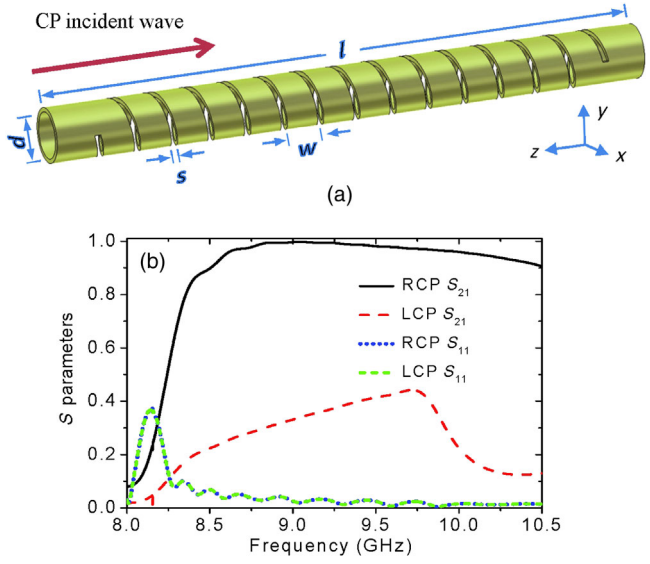

FIG. 1. (a) Schematic diagram of the proposed HTW. The geometric parameters of the HTW are diameter $d = 21.6$ mm, metallic copper thickness $t = 0.5$ mm, slit width $s = 4$ mm, metallic width $w = 15$ mm, lattice constant $a = s + w = 19$ mm, and the number of turns $n = 14$, which corresponds to a length of $l = 290$ mm. (b) Simulated transmission S_{21} and reflection S_{11} for LCP and RCP incident waves.

Figure 1(b) displays the transmission S_{21} and reflection S_{11} for LCP and RCP incident waves. The HTW operates above ~8.3 GHz as a transmission line for the RCP wave given the high transmission and low reflection observed. For the LCP wave, however, transmission and reflection are simultaneously low in the frequency span displayed. The fact that both RCP and LCP waves have almost identical S_{11} indicates that the HTW operates as a leaky-wave antenna for the LCP wave. This antenna operation mode is easily modulated by the values of the slit width s and the helix turns n, while the transmission-line operation mode remains unaffected by these parameters [51]; transmission decreases (i.e., leakage increases) with an increasing slit width s or an increasing number of turns n. This initial study shows that the HTW can transmit the CP light with the same handedness as its helix but partly transmit or even block the other handedness within the same bandwidth. Hence, the proposed HTW can be used to distinguish the circular handedness of an incident electromagnetic wave. Some engineering of the HTW parameters would allow for further improvement of the difference in transmittances of LCP and RCP waves.

In order to show the underlying physics of the circular-polarization-selective transmission of the HTW, Fig. 2(a) displays the simulated electric-field distributions of the HTW at the $z = 0$ plane (i.e., the middle plane of the HTW) for LCP and RCP incident waves at 9 GHz. It can be observed that little radiation occurs for the RCP incident wave. In contrast to the weak radiation of the RCP incident case, significant leakage radiation occurs for the LCP incident case. Interestingly, such leakage radiation forms a vortex. These results show unambiguously that the wave front of the leaky waves is indeed helical and it carries an orbital angular momentum for the LCP incident case. In other words, the coupling between spin angular momentum and orbital angular momentum produces spin-to-orbital angular momentum conversions—helicity-dependent vortex. To study clearly this helicity-dependent radiation, Fig. 2(b) presents the electric-field distributions on the $x = 0$ middle plane at the frequency of 9 GHz. It can be seen that the power is well confined in the HTW for RCP incident wave and little radiation can be observed, resulting in a very high transmission, and therefore, a transmission-line operation. In contrast, when the LCP wave is incident onto the HTW, the power largely leaks through the slits and radiates to free space, leading to a low transmission for the LCP incident wave. These results are consistent with the transmission spectra shown in Fig. 1(b).

Below, we provide an interpretation for this circular-polarization-selective behavior of our HTW and the helicity-dependent radiation. The electromagnetic field and its excitation surface current density in the HTW are both in periodical distribution, due to the azimuthal periodicity and helical symmetry of the tape helix, and consist in space harmonics according to the Floquet theorem [52]. When the

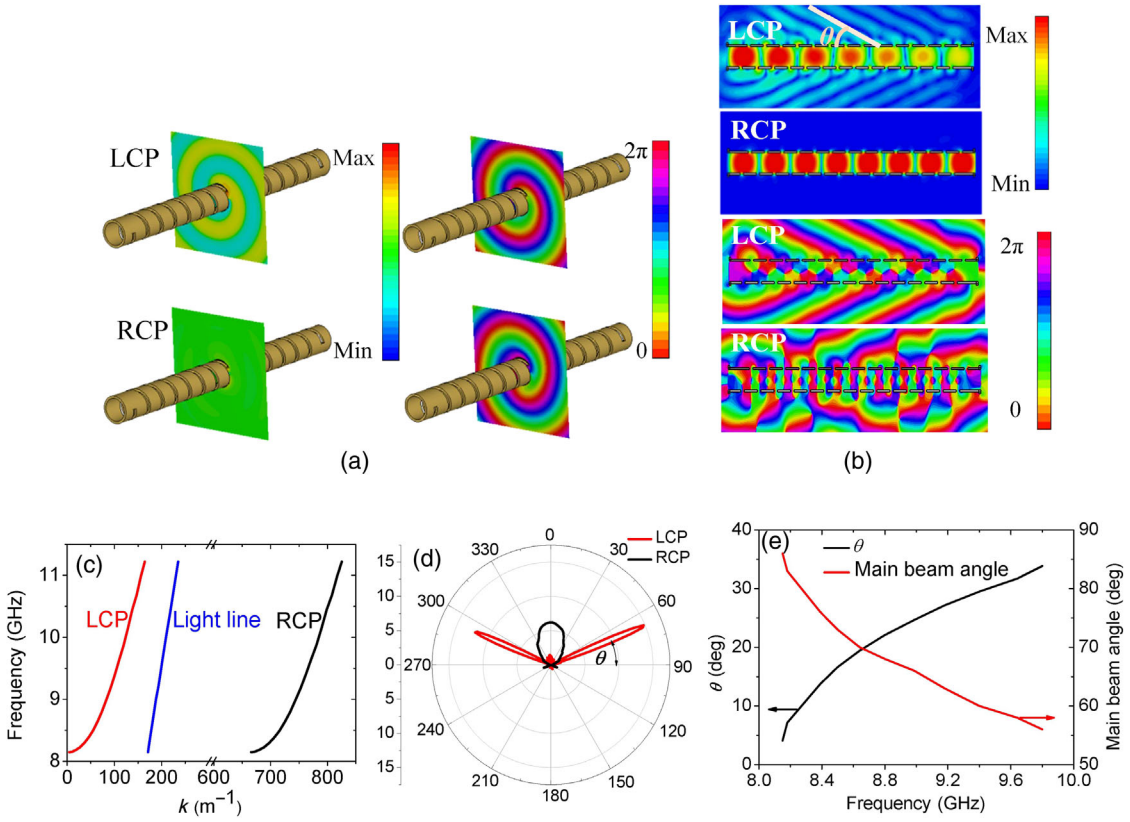

FIG. 2. (a) Electric-field intensity (left) and phase (right) distributions at $z = 0$ plane for LCP and RCP incident waves at 9 GHz. (b) Electric-field intensity (top) and phase (bottom) distributions at the $x = 0$ plane for LCP and RCP incident waves at 9 GHz. (c) Wave vector on the surface of the HTW for LCP and RCP incident waves. (d) Simulated far-field radiation patterns ($\phi = 90°$, linear scale) for LCP and RCP incident waves at 9 GHz. (e) Angle θ and main beam direction versus frequency for the LCP incident case.

propagation wave is circularly polarized, the propagation wave vector of the first space harmonic on the surface of the HTW is $k_1^\sigma = k_z + \sigma[(2\pi)/a] + [(2\pi)/a]$, where k_z is the propagation wave vector of the mode inside the unperturbed waveguide, $\sigma = \pm 1$ is the spin of the incident wave, and $+$ and $-$ represent RCP and LCP, respectively. The second term $2\pi\sigma/a$ on the right side of the equation comes from the SOC; due to the angular momentum conservation, the spin angular momentum of the circularly polarized waveguide mode is converted to the orbital angular momentum of the outgoing beam [53]. The third term $2\pi/a$ is due to the periodical helical structure of the slits.

With the above in-line expression, we calculate the value of k_1^σ as shown in Fig. 2(c). It can be seen that k_1^{+1} is much larger than the free-space wave vector k_0 for the RCP incident wave case, resulting in no leakage radiation. This scenario corresponds to the well-known slow-wave structure widely used in traveling-wave tubes [52]. In contrast, k_1^{-1} is smaller than k_0 for the LCP incident wave, which leads to the leakage radiation with a conical pattern. These behaviors are corroborated in the far-field radiation patterns shown in Fig. 2(d). Notice that 0° corresponds to the waveguide axial direction. For the LCP incident wave, the main-lobe radiation directions are at 66.5° and 293.5°, respectively (i.e., conical mode), at 9 GHz. The far-field radiation pattern for RCP shows, in contrast, the main lobe at 0° (i.e., axial mode). Notice that the conical mode has a more directive beam than the axial mode, as expected from its larger effective radiation length.

Since $k_1^{-1} < k_0$ for the LCP incident wave, the propagation phase velocity is larger than that of free space, and thus, wakes are generated [35] at an angle θ [see Fig. 2(b) for definition] that follows the Cherenkov equation: $\theta = \arcsin[(\omega/k_0)/(\omega/k_1^{-1})] = \arcsin[(k_1^{-1})/(k_0)]$, see Fig. 2(e). Notice that θ increases with frequency. This response is characteristic of a forward leaky-wave antenna [54] whose main beam direction is perpendicular to the wave-front direction. Moreover, as shown in Fig. 2(a), the leakage radiation forms a vortex (i.e., the wave front of the leaky wave is helical), akin to the helical Cherenkov radiation in charge particle experiments.

III. EXPERIMENTS

To verify the observations from the previous section, we fabricate HTW samples. The samples are fabricated by using a circular resin pipe with a diameter of $d = 21.6$ mm wrapped with copper foil with the width of $w = 15$ mm,

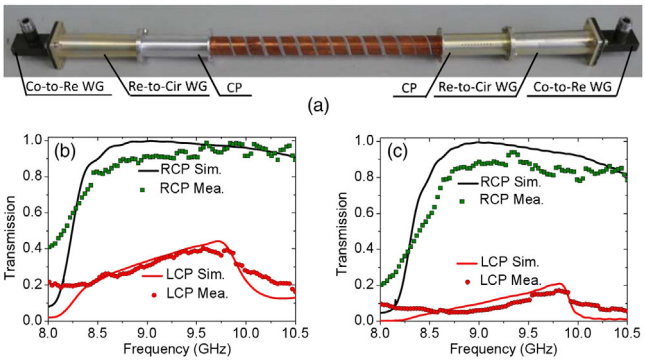

FIG. 3. (a) Experimental setup for transmission S_{21} measurement. The transmission spectra for the HTW with (b) $n = 14$ and (c) $n = 30$. Solid curves indicate the simulations and color symbols represent the measured results.

the thickness of $t = 0.5$ mm, the slit width of $s = 4$ mm, and the lattice constant of $a = s + w = 19$ mm. Two different HTW samples are fabricated with helix turns of $n = 14$ and $n = 30$, corresponding to lengths of $l = 290$ mm and 600 mm, respectively. As shown in Fig. 3(a), the experimental setup for transmission measurement consists of two X-band coaxial-to-rectangular waveguide connectors, two rectangular-to-circular waveguide connectors, two circular polarizers, and an AV 3629 vector network analyzer (45 MHz–40 GHz). Two circular polarizers are employed to generate a circularly polarized wave, and the opposite circularly polarized wave can be produced by rotating the two circular polarizers simultaneously by 90°. The network analyzer connecting the two coaxial connectors to its two ports is used to measure LCP and RCP transmissions.

Figures 3(b) and 3(c) show the transmission spectra of the two HTW samples. For both samples, a very high transmission is observed for the RCP incident electromagnetic wave, whereas low transmission is detected for the LCP incident wave (the longer the sample, the lower the transmission), as expected from our previous discussion. Namely, for the LCP case, the transmission coefficient is 0.32 and 0.061 at 9 GHz for the HTW samples with $n = 14$ and $n = 30$, respectively. Since conductive loss can be neglected, these values yield to a leakage constant $\alpha = 3.78$ Np/m ($\alpha/k_0 = 0.02$), and 3.59 Np/m ($\alpha/k_0 = 0.019$) at 9 GHz for the HTW samples with $n = 14$ and $n = 30$, respectively. The slight difference in the leakage constant can arguably be assigned to truncation effects due to the finite size of the waveguide. The leakage constant α versus

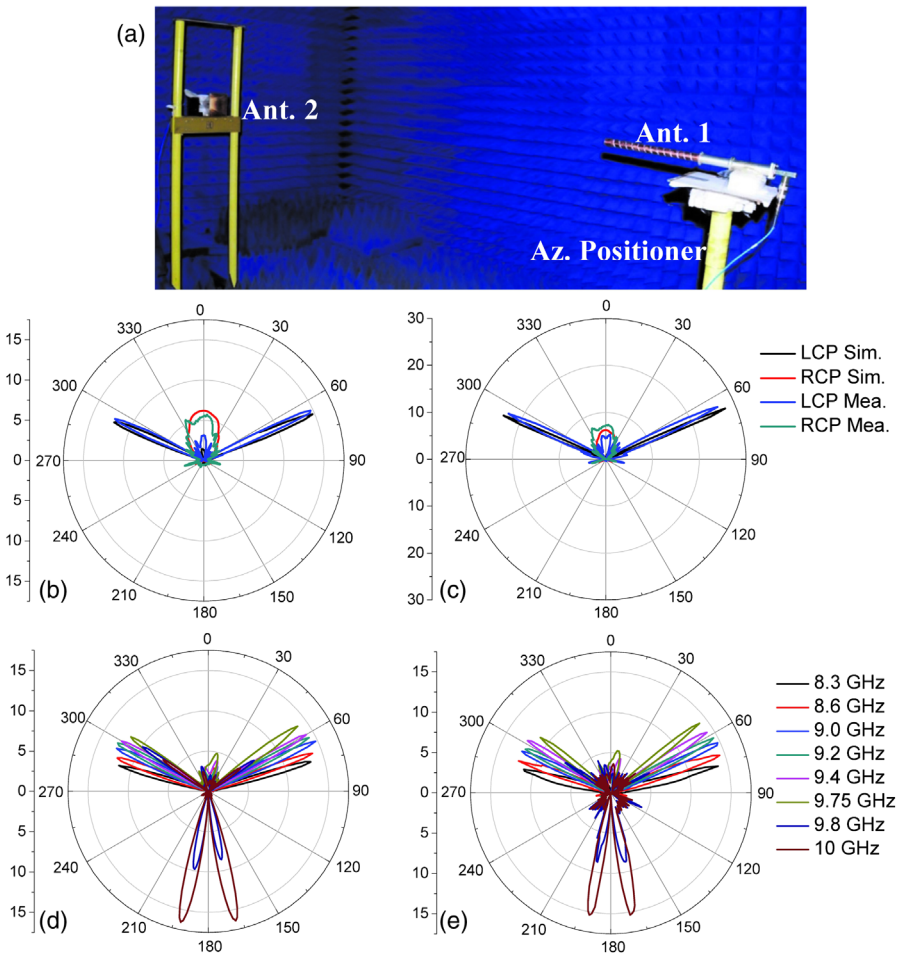

FIG. 4. (a) Experimental setup in an anechoic chamber, and the simulated and measured far-field radiation patterns ($\phi = 90°$, linear scale) for the HTW samples with (b) $n = 14$ and (c) $n = 30$ at 9 GHz. (d) Simulated and (e) measured far-field radiation patterns ($\phi = 90°$, linear scale) of the HTW sample with $n = 14$ at various frequencies for the LCP incident wave.

frequency is shown in Ref. [51]. The experimental results (color symbols) show a good agreement with the simulations (solid curves). For both samples, a large transmittance ratio is observed at a broadband frequency range from 8.3 to 9.75 GHz, which corresponds to a fractional bandwidth of 16.1%. The measured reflections are low both for LCP and RCP waves [51], which agrees with the simulations. Our results thus manifest that the HTW can transmit almost completely the circular polarization wave with the same helicity as its helix slit, whereas it partly transmits or even blocks the opposite one over a broadband frequency range.

The far-field radiation patterns of both samples are also investigated experimentally. These measurements are carried out in an anechoic chamber with an AV 3629 vector network analyzer, and a standard X-band linearly polarized horn antenna. As shown in Fig. 4(a), the fabricated HTW (antenna 1) is placed on an azimuth positioner serving as an emitter and the standard X-band linearly polarized horn antenna (antenna 2) serves as a receiver. An X-band coaxial-to-rectangular waveguide connector, a rectangular-to-circular waveguide connector, and a circular polarizer feed the HTW to generate a CP wave.

Figures 4(b) and 4(c) display the far-field radiation patterns of the HTW with $n = 14$ and $n = 30$, respectively. For the HTW with $n = 14$, the far-field radiation pattern for the LCP incident wave shows that the measured main-lobe radiation directions are centered at 65.2° and 294.8° at 9 GHz, respectively. The maximum measured magnitude of the main lobes is 14.7 (11.7 dB) due to the leakage radiation. The measured radiation pattern is in a good agreement with the simulation, with a deviation of only ∼1.3° in the main-lobe directions. As compared with the LCP case, the far-field radiation pattern for the RCP incident wave shows a wider main lobe at 0° whose magnitude is ∼6 (7.8 dB). This is due to the fact that little power of this mode is radiated. Similar results are observed with $n = 30$ in Fig. 4(c), except that the measured magnitude of the main lode is 26.5 (14.2 dB) for the LCP incident case because of the longer leakage length. All of these far-field radiation patterns are consistent with the preceding studies of the transmission spectra and the electric-field distributions.

Finally, Figs. 4(d) and 4(e) present the frequency response of the simulated and measured far-field radiation patterns of the HTWs with $n = 14$ for the LCP incidence wave, respectively. It is shown that the main-lobe direction moves from near broadside toward forward end-fire as the frequency increases. The measured directions of the main lobes are consistent with the simulations. It is worth noting that at the top end of the frequency scan (9.8 and 10 GHz), the higher-order space harmonic emerges with the beam direction pointing very close to the backward end-fire. Similar results are obtained for the HTW sample with $n = 30$, except that the main-lobe magnitude is larger than that of the HTW sample with $n = 14$.

IV. CONCLUSIONS

To conclude, we have designed and fabricated a HTW structure to achieve a strong asymmetry between the circular polarizations of the transmitted electromagnetic wave. We demonstrate numerically and experimentally that the circular-polarization-selective property of the HTW is due to the SOC. Transmission spectra, electric-field distributions, and far-field radiation patterns show that a RCP electromagnetic wave propagates through the HTW with negligible radiation over a broadband frequency range. The HTW operates as a slow-wave structure for the RCP incident wave. In contrast, low transmission is obtained and a significant leakage radiation is observed for the LCP case. The HTW operates in this case as a leaky-wave antenna. Moreover, the leakage radiation forms a vortex, an analogue of a helical Cherenkov radiation for the LCP case. This unique physical phenomenon originates from the fact that the coupling between the spin angular momentum and orbital angular momentum produces spin-to-orbital angular momentum conversions.

ACKNOWLEDGMENTS

Y. L. is supported by the National Natural Science Foundation of China (Grant No. 11204241); the National Aerospace Science Foundation of China (Grant No. 2016ZF53061); the Natural Science Basic Research Plan in Shaanxi Province of China (Grant No. 2017JM1009); the Fundamental Research Funds for the Central Universities (Grant No. 3102017jghk02004); the China Scholarship Council; and the Top International University Visiting Program for Outstanding Young Scholars of Northwestern Polytechnical University. Q. G. acknowledges support from the National Natural Science Foundation of China (Grant No. 11604216). K. S. acknowledges support from the National Natural Science Foundation of China (Grant No. 61601375). S. Z. acknowledges support from European Research Council Consolidator Grant (TOPOLOGICAL); the Royal Society and the Wolfson Foundation; and Horizon 2020 Action, Projects No. 734578 (D-SPA) and No. 648783. M. N.-C. acknowledges support from University of Birmingham (Birmingham Fellowship).

[1] J. Wunderlich, B. Kaestner, J. Sinova, and T. Jungwirth, Experimental Observation of the Spin-Hall Effect in a Two-Dimensional Spin-Orbit Coupled Semiconductor System, Phys. Rev. Lett. **94**, 047204 (2005).

[2] L. W. Cheuk, A. T. Sommer, Z. Hadzibabic, T. Yefsah, W. S. Bakr, and M. W. Zwierlein, Spin-Injection Spectroscopy of a Spin-Orbit Coupled Fermi Gas, Phys. Rev. Lett. **109**, 095302 (2012).

[3] V. Galitski and I. B. Spielman, Spin-orbit coupling in quantum gases, Nature (London) **494**, 49 (2013).

[4] H. Zhai, Degenerate quantum gases with spin-orbit coupling: A review, Rep. Prog. Phys. **78**, 026001 (2015).

[5] C. Cacho, A. Crepaldi, M. Battiato, J. Braun, F. Cilento, M. Zacchigna, M. C. Richter, O. Heckmann, E. Springate, Y. Liu, S. S. Dhesi, H. Berger, Ph. Bugnon, K. Held, M. Grioni, H. Ebert, K. Hricovini, J. Minár, and F. Parmigiani, Momentum-Resolved Spin Dynamics of Bulk and Surface Excited States in the Topological Insulator Bi_2Se_3, Phys. Rev. Lett. **114**, 097401 (2015).

[6] O. Hosten and P. Kwiat, Observation of the spin Hall effect of light via weak measurements, Science **319**, 787 (2008).

[7] K. Y. Bliokh, F. J. Rodríguez-Fortuño, F. Nori, and A. V. Zayats, Spin-orbit interactions of light, Nat. Photonics **9**, 796 (2015).

[8] L. Marrucci, E. Karimi, S. Slussarenko, B. Piccirillo, E. Santamato, E. Nagali, and F. Sciarrino, Spin-to-orbital conversion of the angular momentum of light and its classical and quantum applications, J. Opt. **13**, 064001 (2011).

[9] Q. Guo, W. Gao, J. Chen, Y. Liu, and S. Zhang, Line Degeneracy and Strong Spin-Orbit Coupling of Light with Bulk Bianisotropic Metamaterials, Phys. Rev. Lett. **115**, 067402 (2015).

[10] M. Kang, J. Chen, S. M. Li, B. Gu, Y. Li, and H. T. Wan, Optical spin-dependent angular shift in structured metamaterials, Opt. Lett. **36**, 3942 (2011).

[11] Q. Tan, Q. Guo, H. Liu, X. Huang, and S. Zhang, Controlling the plasmonic orbital angular momentum by combining the geometric and dynamic phases, Nanoscale **9**, 4944 (2017).

[12] H. Zhang, M. Kang, X. Zhang, W. Guo, C. Lv, Y. Li, W. Zhang, and J. Han, Coherent control of optical spin-to-orbital angular momentum conversion in metasurface, Adv. Mater. **29**, 1604252 (2017).

[13] L. Huang, X. Chen, H. Muhlenbernd, G. Li, B. Bai, Q. Tan, G. Jin, T. Zentgraf, and S. Zhang, Dispersionless phase discontinuities for controlling light propagation, Nano Lett. **12**, 5750 (2012).

[14] Y. Yang, W. Wang, P. Moitra, I. I. Kravchenko, D. P. Briggs, and J. Valentine, Dielectric meta-reflectarray for broadband linear polarization conversion and optical vortex generation, Nano Lett. **14**, 1394 (2014).

[15] S. Mei, M. Q. Mehmood, S. Hussain, K. Huang, X. Ling, S. Y. Siew, H. Liu, J. Teng, A. Danner, and C. W. Qiu, Flat helical nanosieves, Adv. Funct. Mater. **26**, 5255 (2016).

[16] M. D. Turner, M. Saba, Q. Zhang, B. P. Cumming, G. E. Schroder-Turk, and M. Gu, Miniature chiral beamsplitter based on gyroid photonic crystals, Nat. Photonics **7**, 801 (2013).

[17] M. Khorasaninejad and K. B. Crozier, Silicon nanofin grating as a miniature chirality-distinguishing beam-splitter, Nat. Commun. **5**, 5386 (2014).

[18] Z. Li, E. Palacios, S. Butun, and K. Aydin, Visible-frequency metasurfaces for broadband anomalous reflection and high-efficiency spectrum splitting, Nano Lett. **15**, 1615 (2015).

[19] Y. Zhang, L. Zhou, J. Li, Q. Wang, and C. Huang, Ultra-broadband and strongly enhanced diffraction with metasurfaces, Sci. Rep. **5**, 10119 (2015).

[20] M. Kenney, S. Li, X. Zhang, X. Su, T. Kim, D. Wang, D. Wu, C. Ouyang, J. Han, W. Zhang, H. Sun, and S. Zhang, Pancharatnam–Berry phase induced spin-selective transmission in herringbone dielectric metamaterials, Adv. Mater. **28**, 9567 (2016).

[21] W. Ye, X. Yuan, C. Guo, J. Zhang, B. Yang, and S. Zhang, Large Chiroptical Effects in Planar Chiral Metamaterials, Phys. Rev. Applied **7**, 054003 (2017).

[22] K. Y. Bliokh, Y. Gorodetski, V. Kleiner, and E. Hasman, Coriolis Effect in Optics Unified Geometric Phase and Spin-Hall Effect, Phys. Rev. Lett. **101**, 030404 (2008).

[23] O. G. Rodríguez-Herrera, D. Lara, K. Y. Bliokh, E. A. Ostrovskaya, and C. Dainty, Optical Nanoprobing via Spin-Orbit Interaction of Light, Phys. Rev. Lett. **104**, 253601 (2010).

[24] Y. Gorodetski, A. Niv, V. Kleiner, and E. Hasman, Observation of the Spin-Based Plasmonic Effect in Nanoscale Structures, Phys. Rev. Lett. **101**, 043903 (2008).

[25] S. S. Kruk, M. Decker, I. Staude, S. Schlecht, M. Greppmair, D. N. Neshev, and Y. S. Kivshar, Spin-polarized photon emission by resonant multipolar nanoantennas, ACS Photonics **1**, 1218 (2014).

[26] L. T. Vuong, A. J. L. Adam, J. M. Brok, P. C. M. Planken, and H. P. Urbach, Electromagnetic Spin-Orbit Interactions via Scattering of Subwavelength Apertures, Phys. Rev. Lett. **104**, 083903 (2010).

[27] L. Marrucci, C. Manzo, and D. Paparo, Optical Spin-to-Orbital Angular Momentum Conversion in Inhomogeneous Anisotropic Media, Phys. Rev. Lett. **96**, 163905 (2006).

[28] N. Shitrit, I. Yulevich, E. Maguid, D. Ozeri, D. Veksler, V. Kleiner, and E. Hasman, Spin-optical metamaterial route to spin-controlled photonics, Science **340**, 724 (2013).

[29] S. Y. Lee, I. M. Lee, J. Park, S. Oh, W. Lee, K. Y. Kim, and B. Lee, Role of Magnetic Induction Currents in Nanoslit Excitation of Surface Plasmon Polaritons, Phys. Rev. Lett. **108**, 213907 (2012).

[30] F. J. Rodríguez-Fortuño, G. Marino, P. Ginzburg, D. O'Connor, A. Martínez, G. A. Wurtz, and A. V. Zayats, Near-feld interference for the unidirectional excitation of electromagnetic guided modes, Science **340**, 328 (2013).

[31] J. Petersen, J. Volz, and A. Rauschenbeutel, Chiral nanophotonic waveguide interface based on spin-orbit interaction of light, Science **346**, 67 (2014).

[32] R. Mitsch, C. Sayrin, B. Albrecht, P. Schneeweiss, and A. Rauschenbeutel, Quantum state-controlled directional spontaneous emission of photons into a nanophotonic waveguide, Nat. Commun. **5**, 5713 (2014).

[33] B. le Feber, N. Rotenberg, and L. Kuipers, Nanophotonic control of circular dipole emission, Nat. Commun. **6**, 6695 (2015).

[34] I. Söllner, S. Mahmoodian, S. L. Hansen, L. Midolo, A. Javadi, G. Kiršanskė, T. Pregnolato, H. El-Ella, E. H. Lee, J. Song, S. Stobbe, and P. Lodahl, Deterministic photon–emitter coupling in chiral photonic circuits, Nat. Nanotechnol. **10**, 775 (2015).

[35] P. Genevet, D. Wintz, A. Ambrosio, A. She, R. Blanchard, and F. Capasso, Controlled steering of Cherenkov surface plasmon wakes with a one-dimensional metamaterial, Nat. Nanotechnol. **10**, 804 (2015).

[36] J. J. Aubert, U. Becker, P. J. Biggs, J. Burger, M. Chen, G. Everhart, P. Goldhagen, J. Leong, T. McCorriston, T. G. Rhoades, M. Rohde, S. C. Ting, S. L. Wu, and Y. Y. Lee, Experimental Observation of a Heavy Particle *J*, Phys. Rev. Lett. **33**, 1404 (1974).

[37] M. Danos, S. Geschwind, H. Lashinksky, and A. Vantrier, Cerenkov effect at microwave frequencies, Phys. Rev. **92**, 828 (1953).

[38] D. H. Auston, K. P. Cheung, J. A. Valdmanis, and D. A. Kleinman, Cherenkov Radiation from Femtosecond Optial Pulses in Electro-Optics Media, Phys. Rev. Lett. **53**, 1555 (1984).

[39] V. Ginis, J. Danckaert, I. Veretennicoff, and P. Tassin, Controlling Cherenkov Radiation with Transformation-Optical Metamaterials, Phys. Rev. Lett. **113**, 167402 (2014).

[40] M. A. Shapiro, S. Trendafilov, Y. Urzhumov, A. Alu, R. J. Temkin, and G. Shvets, Active negative-index metamaterial powered by an electron beam, Phys. Rev. B **86**, 085132 (2012).

[41] D. M. French, D. Shiffler, and K. Cartwright, Electron beam coupling to a metamaterial structure, Phys. Plasmas **20**, 083116 (2013).

[42] Y. P. Bliokh, S. Savel'ev, and F. Nori, Electron-Beam Instability in Left-Handed Media, Phys. Rev. Lett. **100**, 244803 (2008).

[43] Z. Duan, B. I. Wu, J. Lu, J. A. Kong, and M. Chen, Reversed Cherenkov radiation in unbounded anisotropic double-negative metamaterials, J. Phys. D **42**, 185102 (2009).

[44] J. S. Hummelt, X. Lu, H. Xu, I. Mastovsky, M. A. Shapiro, and R. J. Temkin, Coherent Cherenkov-Cyclotron Radiation Excited by an Electron Beam in a Metamaterial Waveguide, Phys. Rev. Lett. **117**, 237701 (2016).

[45] S. Xi, H. Chen, T. Jiang, Li. Ran, J. Huangfu, B. I. Wu, J. A. Kong, and M. Chen, Experimental Verification of Reversed Cherenkov Radiation in Left-Handed Metamaterial, Phys. Rev. Lett. **103**, 194801 (2009).

[46] J. K. So, J. H. Won, M. A. Sattorov, S. H. Bak, K. H. Jang, G. S. Park, D. S. Kim, and F. J. Garcia-Vidal, Cerenkov radiation in metallic metamaterials, Appl. Phys. Lett. **97**, 151107 (2010).

[47] J. Soln, Helical Cerenkov effect, a novel radiation source, IEEE Trans. Plasma Sci. **22**, 526 (1994).

[48] J. Soln, The helical Cerenkov effect with a non-mono-energetic electron beam, J. Phys. D **30**, 2936 (1997).

[49] J. D. Kraus and J. C. Williamson, Characteristics of helical antennas radiating in the axial mode, J. Appl. Phys. **19**, 87 (1948).

[50] A. R. Neureuther, P. W. Klock, and R. Mittra, A study of the sheath helix with a conducting core and its application to the helical antenna, IEEE Trans. Antennas Propag. **15**, 203 (1967).

[51] See Supplemental Material at http://link.aps.org/supplemental/10.1103/PhysRevApplied.9.054033 for the effect of slit width and number of turns on the transmission, reflection and radiation pattern, leakage constant vs frequency, and measured reflection spectra.

[52] R. E. Collin, *Field Theory of Guided Waves*, 2nd ed. (Wiley-IEEE Press, Piscataway, 1990), Chap. 9, pp. 605–644.

[53] M. Kang, J. Chen, X. L. Wang, and H. T. Wang, Twisted vector field from an inhomogeneous and anisotropic metamaterial, J. Opt. Soc. Am. B **29**, 572 (2012).

[54] U. Beaskoetxea, S. Maci, M. Navarro-Cía, and M. Beruete, 3-D-printed 96 GHz Bull's-eye antenna with off-axis beaming, IEEE Trans. Antennas Propag. **65**, 17 (2017).